Eye-in-Hand Visual Servoing of Concentric Tube Robots

Andrey V. Kudryavtsev*, Mohamed Taha Chikhaoui*, *Member, IEEE*, Aleksandr Liadov, Patrick Rougeot, Fabien Spindler, Kanty Rabenorosoa, *Member, IEEE*, Jessica Burgner-Kahrs, *Member, IEEE*, Brahim Tamadazte, *Member, IEEE*, and Nicolas Andreff, *Member, IEEE*

***Abstract*—This paper deals with the development of a vision-based controller for a continuum robot architecture. More precisely, the controlled robotic structure is based on three-tube concentric tube robot (CTR), an emerging paradigm to design accurate, miniaturized, and flexible endoscopic robots. This approach has grown considerably in the recent years finding applications in numerous surgical disciplines. In contrast to conventional robotic structures, CTR kinematics arise many challenges for an optimal control such as friction, torsion, shear, and non-linear constitutive behavior. In fact, in order to ensure efficient and reliable control, in addition to computing an analytical and complete kinematic model, it is also important to close the control loop. To do this, we developed an eye-in-hand visual servoing scheme using a millimeter-sized camera embedded at the robot's tip.**

Both the kinematic model and the visual servoing controller were successfully validated in simulation with ViSP (Visual Servoing Platform) and using an experimental setup. The obtained results showed satisfactory performances for 3-degrees of freedom positioning and path following tasks with adaptive gain control.

***Index Terms*—concentric tube robot, eye-in-hand visual servoing, CTR kinematics, model-based control, medical application.**

I. Introduction

MEDICAL robotics evolved more and more towards MIS (Minimally Invasive Surgery) and NOTES (Natural Orifice Transluminal Endoscopic Surgery) over the last ten years. Recent developments show particular interest in continuum robots (CR) and concentric tube robots (CTR), in particular [1]. Indeed, CTR paradigm provides a high level of dexterity in confined spaces and enables to push the limits of miniaturization further [2] compared to cable or tendon driven CR [3], fluidic [4] or smart actuator based CR [5], [6]. Several developments concern medical applications such as endonasal surgery, cardiac surgery, pulmonary surgery as reviewed in [1]. To achieve medical tasks, CTR can be teleoperated through a surgeon-robot interface or closed-loop controlled using exteroceptive sensors as stereo camera [7], magnetic resonnance imaging [8], computed tomography [9], ultrasounds [10], or more recently Optical Coherence Tomography (OCT) [11] in an eye-to-hand configuration (when the camera views simultaneously both the robot and the scene). Some tasks require visual feedback to perform an automatic repetitive biopsy to follow-up cell evolution [12], achieve path following in the image [13], and keep a tool in the field-of-view [10], [14] during interventions. In addition, the development of surgical robotic systems with two CR is increasing [15], [16]. In this case, the first CR brings a tool and the second one embeds the visualization system with a diameter smaller than 2 mm, e.g., miniaturized camera, OCT probe, or probe-based confocal laser endomicroscopy. An eye-in-hand configuration, i.e. a visual sensor mounted on the tip of the robot, is well suited to achieve the control of CR in endoscopic interventions. In contrast to a static camera, this configuration allows easier target recognition and inspection resulting from localization, resolution of occlusion problem and limited depth-of-field, as well as spatial resolution [17]. As a result, with visual feedback, one can imagine task autonomy under the supervision of surgeons or physicians in order to improve safety, accuracy, and reduce the intervention duration. To close the control loop, one can consider an image-based visual servoing (IBVS) scheme.

A model-free IBVS technique is proposed in [18], [19] allowing to control the motion of a CTR limited to two and four degrees-of-freedom (DOF) respectively (i.e. composed of 2 tubes). Authors proposed the use of an estimated Jacobian matrix which has to be updated for each cycle.

In this paper, we propose an IBVS for CTR in eye-in-hand configuration. The advantage of this approach is based on the accurate calculation of both the robot Jacobian and the interaction matrix which enables to perform task redundancy control [20], [21]. The main contribution of this paper consists of the model-based eye-in-hand visual servoing of CTR, which includes the derivation of the visual servoing method and its implementation in the Visual Servoing Platform (ViSP) [22] by using a complete model of three tube CTR. In addition, 6 DOF visual servoing simulation results and 3 DOF experimental results with adaptive control gain and tracking scenario for

Manuscript received: September, 10, 2017; Revised December, 2, 2017; Accepted January, 27, 2018.

This paper was recommended for publication by Editor Antonio Bicchi upon evaluation of the Associate Editor and Reviewers' comments.

This work was supported by the Labex ACTION project (contract "ANR-11-LABX-0001-01") and ANR NEMRO (contract 'ANR-14-CE17-0013"). This work was partially supported by the German Research Foundation Emmy Noether Research Grant (BU 2935/1-1)

*These authors contributed equally to this work

A. V. Kudryavtsev, A. Liadov, P. Rougeot, K. Rabenorosoa, N. Andreff, and B. Tamadazte are with FEMTO-ST Institute, Univ. Bourgogne Franche-Comté, CNRS, F-25000 Besançon, France rkanty@femto-st.fr

F. Spindler is with the Inria Rennes-Bretagne Atlantique, Campus universitaire de Beaulieu, Rennes 35042, France fabien.spindler@inria.fr

M. T. Chikhaoui and J. Burgner-Kahrs are with the Laboratory for Continuum Robotics, Leibniz Universitaet Hannover, Appelstr. 11, 30167 Hanover, Germany chikhaoui@lkr.uni-hannover.de

free-space positioning are presented.

This paper is organized as follows. Section II introduces briefly the IBVS control scheme for the eye-in-hand configuration, while Section III details the three tubes CTR modeling and its implementation in ViSP library. Section IV presents the experimental validation of the proposed method.

II. Methods for Eye-in-Hand Visual Servoing

This section is devoted to the brief introduction of IBVS control in eye-in-hand configuration and the derivation of the control law by considering a model-based approach.

A. Basics of Visual Servoing

The aim of a conventional image-based control scheme is to minimize an error $\mathbf{e}(t)$, which is typically defined by

$$\mathbf{e}(t) = \mathbf{s}(\mathbf{m}(t), \mathbf{a}) - \mathbf{s}^* \tag{1}$$

where $\mathbf{m}(t)$ is a set of image measurements (e.g., geometric visual features like 2D points, segments, lines, etc.) and $\mathbf{a}$ is a set of parameters that represent potential additional knowledge about the system. These image measurements are used to compute a vector of k visual features, $\mathbf{s}(\mathbf{m}(t), \mathbf{a})$. The vector $\mathbf{s}^*$ contains the set of desired values of these visual features.

For now, we consider the case of controlling the motion of a camera with 6 DOF attached to the robot's end-effector. The nature of the visual feature set $\mathbf{s}$ can be used as a classifying means. While the literature is broad on this subject and the community is constantly innovating, one can find the examples of usage of image key-points [23], lines [24], photometric visual servoing [25], [26], and more recently shearlet [27] and wavelet [28] for image-guided investigations in case of medical robotics purposes.

Let the spatial velocity of the camera be denoted by $\mathbf{v}_c$=$[\mathbf{v}, \boldsymbol{\omega}]^\top$ with $\mathbf{v} = [v_x, v_y, v_z]^\top$ the instantaneous linear velocity of the origin of the camera frame and $\boldsymbol{\omega} = [\omega_x, \omega_y, \omega_z]^\top$ the instantaneous angular velocity of the camera frame. Finally, the relationship between $\mathbf{e}$ and $\mathbf{v}_c$ is given by

$$\dot{\mathbf{e}} = \mathbf{L}_\mathbf{s} \mathbf{v}_c \tag{2}$$

where $\mathbf{L}_\mathbf{s} \in \mathbb{R}^{6\times k}$ is called *interaction matrix* related to $\mathbf{s}$.

The most common approach to IBVS is to merely use equations (2) and (1) to construct the control law of the following form

$$\mathbf{v}_c = -\lambda \widehat{\mathbf{L}_\mathbf{s}^+} \big(\mathbf{s}(t) - \mathbf{s}^*\big) \tag{3}$$

where λ is a positive gain and $\widehat{\mathbf{L}_\mathbf{s}^+}$ is the Moore-Penrose pseudo-inverse of the interaction matrix $\mathbf{L}_\mathbf{s}$.

B. Eye-In-Hand Configuration

Equation (3) corresponds to camera velocity that now needs to be transformed to joint velocities. Hence, we use the following control law

$$\dot{\mathbf{q}} = -\lambda (\widehat{\mathbf{L}_\mathbf{s}} {}^c\mathbf{V}_e \, {}^e\mathbf{J}_e)^+ \big(\mathbf{s}(t) - \mathbf{s}^*\big) \tag{4}$$

where ${}^e\mathbf{J}_e$ is robot Jacobian matrix expressed in the end-effector reference frame and ${}^c\mathbf{V}_e$ is the velocity twist matrix of the following form

$${}^c\mathbf{V}_e = \begin{bmatrix} {}^c\mathbf{R}_e & [{}^c\mathbf{t}_e]_\times {}^c\mathbf{R}_e \\ \mathbf{0}_{3\times 3} & {}^c\mathbf{R}_e \end{bmatrix} \tag{5}$$

which is used to transform a velocity skew vector from the end-effector frame $\mathcal{R}_e$ to the camera frame $\mathcal{R}_c$. The product $\widehat{\mathbf{L}_\mathbf{s}} {}^c\mathbf{V}_e \, {}^e\mathbf{J}_e$ is called task-Jacobian. In the following section, the derivation of the CTR kinematics, as well as the Jacobian matrix are provided.

Let us consider $\mathbf{s} = \mathbf{x} = (x, y)$ as the image-plane coordinates of a set of points. For a 3D point with coordinates $\mathbf{P} = (X, Y, Z)$ in the camera frame, which projects as a 2D point with coordinates $\mathbf{x} = (x, y)$, we obtain the projection equations.

$$\begin{cases} x = \dfrac{X}{Z} = (u - c_u)/f\alpha \\ \\ y = \dfrac{Y}{Z} = (v - c_v)/f\alpha \end{cases} \tag{6}$$

where (u, v) gives the coordinates of the image point expressed in pixel units. c_u and c_v are the coordinates of the principal point, f is the focal length, α is the ratio of the pixel dimensions. The interaction matrix $\mathbf{L}_\mathbf{s}$ related to $\mathbf{x}$ is

$$\mathbf{L}_\mathbf{s} = \begin{pmatrix} \frac{-1}{Z} & 0 & \frac{x}{Z} & xy & -(1+x^2) & y \\ 0 & \frac{-1}{Z} & \frac{y}{Z} & 1+y^2 & -xy & -x \end{pmatrix} \tag{7}$$

In the matrix $\mathbf{L}_\mathbf{s}$, the value Z is the depth of the point relative to the camera frame. Therefore, any control scheme that uses this form of the interaction matrix must estimate or approximate the value of Z which can be estimated at the desired position (i.e., Z^*).

III. CTR modeling and implementation in ViSP Library

A. CTR Modeling

In this section, the kinematic modeling of CTR under piecewise constant curvature assumption (PCCA) is presented in order to develop the geometric model, as well as the differential kinematics. The modeling approach, detailed in [29], [30], assumes that for a CTR constituted of n overlapping tubes, one can decompose the final shape into m successive segments. Each of them is assimilated to an arc of a circle by considering the PCCA. The proposed continuum robot joint parameters are called configuration space of arc parameters (κ, ϕ, ℓ) where κ is the curvature, ϕ is the arc equilibrium plane angle, and ℓ is the arc length. The relationship $\theta = \kappa\ell$ defines the bending angle of the arc. Fig. 1 summarizes these parameters and presents the definition of the different axes.

Depending on the overlapping of the n tubes, the curvature of a segment $j \in \{1...m\}$ is given by

$$\kappa_j = \sqrt{\kappa_{x_j}^2 + \kappa_{y_j}^2} \tag{8}$$

with

$$\begin{cases} \kappa_{x_j} = \frac{\sum_{i=1}^{n} E_i I_i \kappa_{i,j} c\theta_{i,j}}{\sum_{i=1}^{n} E_i I_i} \\ \kappa_{y_j} = \frac{\sum_{i=1}^{n} E_i I_i \kappa_{i,j} s\theta_{i,j}}{\sum_{i=1}^{n} E_i I_i} \end{cases} \tag{9}$$

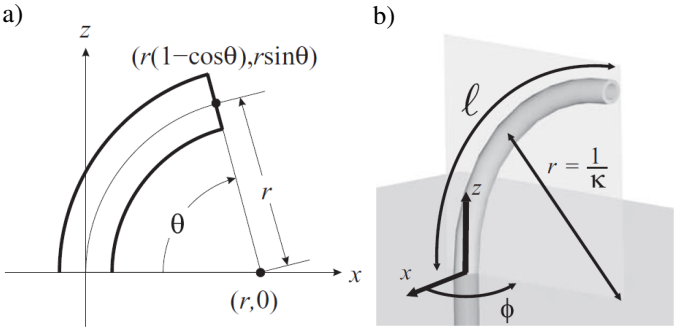

Fig. 1. a) The xz plane definition, when ϕ is zero. r designates the arc radius where $\kappa = 1/r$. b) Definition of the configuration space parameters, where the z- axis is defined as the arc's principal axis [29].

where κ_x and κ_y are the decomposition of the main curvature along the x and y axes, respectively, E_i is the elastic modulus, I_i is the cross sectional moment of inertia, $\kappa_{i,j}$ is the intrinsic curvature of the i$^{\text{th}}$ tube in the j$^{\text{th}}$ segment, and $\theta_{i,j}$ denotes the i$^{\text{th}}$ tube angle about the j$^{\text{th}}$ segment frame z axis, and c and s are cosine and sine functions respectively. The equilibrium plane angle is given by

$$\phi_j = \arctan(\kappa_{y_j}/\kappa_{x_j}) \tag{10}$$

A segment is defined whenever the number of the overlapping tubes is modified or the shape of a tube is different (straight or curved). The configuration for the case of three totally curved concentric tubes i (with $i \in \{1..n\}, n = 3$), then three segments j (with $j \in \{1..m\}, m = 3$) is displayed in Fig. III-A.

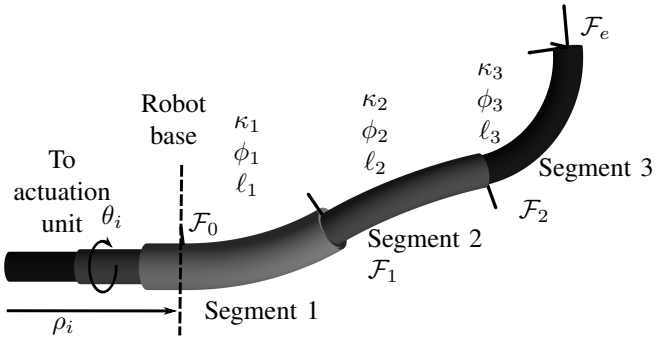

Fig. 2. Schematic description of segment distribution and arc parameters in the presence of three totally curved concentric tubes. The general fixed frame is attached to the outermost tube basis. A coordinate frame $\mathcal{F}_i$ is related to each segment end.

Previously mentioned parameters define the configuration space. In total, three spaces were specified in [31] and can be summarized as follows: the *actuator space* $\{\mathbf{q}_i | i \in \{1..n\}\}$, the *configuration space* $\{\kappa_j, \phi_j, \ell_j | j \in \{1..m\}\}$, and the *task space* in $SE(3)$. Two space transformations are thus defined:

i. The *specific mapping* from the actuator space to the configuration space (actuator dynamics). This mapping totally depends on the actuation of the tubes.
ii. The *independent mapping* from the configuration space to the task space (forward kinematics). This mapping is generic as long as the CR architecture satisfies the PCCA.

The transformation ${}^{j-1}\mathbf{T}_j$ from segment $j-1$ to segment j decomposes into a rotation of center $\mathbf{C}_j = [1/\kappa_j, 0, 0]^T$ about the y axis by θ_j and a rotation about the z axis by ϕ_j:

$${}^{j-1}\mathbf{T}_j = \begin{bmatrix} \mathbf{R}_z(\phi_j) & 0 \\ 0 & 1 \end{bmatrix} \begin{bmatrix} \mathbf{R}_y(\theta_j) & \mathbf{p}_j \\ 0 & 1 \end{bmatrix} \tag{11}$$

$${}^{j-1}\mathbf{T}_j = \begin{bmatrix} c\phi_j c\theta_j & -s\phi_j & c\phi_j s\theta_j & c\phi_j(1-c\theta_j)/\kappa_j \\ s\phi_j c\theta_j & c\phi_j & s\phi_j s\theta_j & s\phi_j(1-c\theta_j)/\kappa_j \\ -s\theta_j & 0 & c\theta_j & s\theta_j/\kappa_j \\ 0 & 0 & 0 & 1 \end{bmatrix} \tag{12}$$

where $\theta_j = \kappa_j \ell_j$ and $\mathbf{p}_j = [r_j(1-c\theta_j), 0, r_j s\theta_j]^\top$.

a) Independent Jacobian Matrix: The independent Jacobian computation relies substantially on the forward kinematics differentiation. The velocity of the j^{th} segment according to segment $(j-1)$ is defined by

$${}^{j-1}\dot{\mathbf{X}}_j = \underbrace{\begin{bmatrix} c\Delta\phi_j(c(\kappa_j\ell_j)-1)/\kappa_j^2 & 0 & 0 \\ s\Delta\phi_j(c(\kappa_j\ell_j)-1)/\kappa_j^2 & 0 & 0 \\ -(s(\kappa_j\ell_j)-\kappa_j\ell_j)/\kappa_j^2 & 0 & 1 \\ -\ell_j s\Delta\phi_j & 0 & -\kappa_j s\Delta\phi_j \\ \ell_j c\Delta\phi_j & 0 & \kappa_j c\Delta\phi_j \\ 0 & 1 & 0 \end{bmatrix}}_{{}^{j-1}\mathbf{J}_{ind_j}} \begin{bmatrix} \dot{\kappa}_j \\ \Delta\dot{\phi}_j \\ \dot{\ell}_j \end{bmatrix} \tag{13}$$

where $\Delta\phi_j = \phi_j - \phi_{j-1}$ for $j \in \{2..m\}$ and $\Delta\phi_1 = \phi_1$.

Based on the adjoint transformation introduced in [32] and used in equation (5), the full independent kinematic Jacobian ${}^{e}\mathbf{J}_{ind_e}$ can be computed in the robot's end-effector frame.

For a configuration with three totally curved CTR, we obtain ${}^{e}\mathbf{J}_{ind_e} \in \mathbb{R}^{6\times 9}$, as m=3 as described in Fig. III-A.

b) Specific Jacobian Matrix: The specific mapping depends essentially on the actuator structure and distribution along the CR. The derivatives of the curvature and equilibrium angle can be expressed with the same structure independently to the actuation. Differentiating (8) and (10) with respect to κ_x and κ_y yields

$$\begin{cases} \dot{\kappa}_j = \frac{1}{\sqrt{\kappa_{x_j}^2+\kappa_{y_j}^2}} \begin{bmatrix} \kappa_{x_j} & \kappa_{y_j} \end{bmatrix} \begin{bmatrix} \dot{\kappa}_{x_j} \\ \dot{\kappa}_{y_j} \end{bmatrix} \\ \dot{\phi}_j = \frac{1}{1+\kappa_{y_j}^2} \begin{bmatrix} -\kappa_{y_j} & \kappa_{x_j} \end{bmatrix} \begin{bmatrix} \dot{\kappa}_{x_j} \\ \dot{\kappa}_{y_j} \end{bmatrix} \end{cases} \tag{14}$$

where $\dot{\kappa}_{x_j}$ and $\dot{\kappa}_{y_j}$ are respectively the derivatives of κ_{x_j} and κ_{y_j} with respect to the actuators used in this case. The actuator space of CTR is defined by $\left\{\mathbf{q} = (\theta_i, .., \theta_n, \rho_i, .., \rho_n)^\top | i \in \{1..n\}\right\}$ where ρ_i and θ_i are the insertion length and angle of the i^{th} tube, respectively.

Differentiating the j^{th} segment's arc parameters leads to:

$$\begin{bmatrix} \dot{\kappa}_j \\ \dot{\phi}_j \end{bmatrix} = \underbrace{\begin{bmatrix} \frac{1}{\sqrt{\kappa_{x_j}^2+\kappa_{y_j}^2}} \begin{bmatrix} \kappa_{x_j} & \kappa_{y_j} \end{bmatrix} \\ \frac{1}{1+\kappa_{y_j}^2} \begin{bmatrix} -\kappa_{y_j} & \kappa_{x_j} \end{bmatrix} \end{bmatrix}}_{\mathbf{x}_j} \mathbf{A}_j \begin{bmatrix} \dot{\theta}_j \\ \vdots \\ \dot{\theta}_m \end{bmatrix} \tag{15}$$

with $\mathbf{A}_j = \frac{1}{\sum_{i=j}^{m} E_i I_i} \begin{bmatrix} -E_i I_i \kappa_{i,i} s\theta_i & \dots & -E_m I_m \kappa_{i,m} s\theta_m \\ E_i I_i \kappa_{i,i} c\theta_i & \dots & E_m I_m \kappa_{i,m} c\theta_m \end{bmatrix}$ for $i \in \{j..m\}$.

To summarize, after adding the segment length derivatives, the final arc parameter derivatives is

$$\begin{bmatrix} \dot{\kappa}_1 \\ \dot{\phi}_1 \\ \dot{\kappa}_2 \\ \dot{\phi}_2 \\ \dot{\kappa}_3 \\ \dot{\phi}_3 \\ \dot{\ell}_1 \\ \dot{\ell}_2 \\ \dot{\ell}_3 \end{bmatrix} = \underbrace{\begin{bmatrix} \mathbf{X}_1 & & & \mathbf{0}_{2\times 3} \\ \mathbf{0}_{2\times 1} & \mathbf{X}_2 & & \mathbf{0}_{2\times 3} \\ \mathbf{0}_{2\times 2} & & \mathbf{X}_3 & \mathbf{0}_{2\times 3} \\ 0 & 0 & 0 & 1 & 0 & 0 \\ 0 & 0 & 0 & -1 & 1 & 0 \\ 0 & 0 & 0 & 0 & -1 & 1 \end{bmatrix}}_{\mathbf{J}_{spec}} \underbrace{\begin{bmatrix} \dot{\theta}_1 \\ \dot{\theta}_2 \\ \dot{\theta}_3 \\ \dot{\rho}_1 \\ \dot{\rho}_2 \\ \dot{\rho}_3 \end{bmatrix}}_{\dot{\mathbf{q}}} \quad (16)$$

with $\mathbf{J}_{spec} \in \mathbb{R}^{9\times 6}$ is the specific Jacobian.

Finally, the full Jacobian matrix ${}^e\mathbf{J}_e$, utilized in equation (4), is calculated such that

$${}^e\mathbf{J}_e = {}^e\mathbf{J}_{ind_e} \mathbf{J}_{spec} \quad (17)$$

B. Implementation of CTR Model in ViSP

ViSP is a modular C++ multi-platform library that allows fast development of visual servoing applications. It was introduced since more than ten years [22] and the latest stable release can be downloaded `here`. The CTR kinematics are implemented in ViSP by following the library structure. Two classes were created based on *vpRobotTemplate*: *vpRobotCTR* and *vpSimulatorRobotCTR*. The contents of these classes is similar, both include the robot parameters and forward kinematics equations. However, the class *vpRobotCTR* further includes the code needed for the interaction with the real robot through UDP (User Datagram Protocol) interface.

1) 3D positioning task: In order to obtain first validation of the model, the tests were performed with the simulator class. The robot needed to perform a simple task of achieving the desired position from different starting points. The simulation target contains four features, which is the minimal configuration needed to find the transformation between two images (similar to the homography estimation [33]). The results of one simulation example of the 6-DOF CTR control are displayed in Fig. 3. The error of the positioning task is calculated as a sum of squared differences between point positions in image frame. Note that the task is considered achieved when the norm of the error reaches the value of 10^{-5} m^2.

2) Adaptive gain for fast convergence: As mentioned previously, the kinematic model of the robot is highly nonlinear. It results in the fact that the impact of each joint variable on the final position of the robot's end-effector is very different. Thus, in order to compensate this effect and to ensure better and faster convergence, the IBVS scheme with adaptive gain is proposed. Indeed, it ensures stability, decreases the time of convergence, avoids overshoot for small errors, and limits the maximum speed [34], [35]. In the following, the value of the gain λ in equation (4) should be different for every joint. Therefore, it transforms to a vector $\boldsymbol{\lambda} = (\lambda_1, ..., \lambda_n)^\top$, containing six entries in our case, with λ_i corresponding to joint variable q_i. The values of λ_i will be determined experimentally. Moreover, we also suggest adding an adjustment function in order to tune the gains according to the error value. It means that the gain should be increased if the pixel error in the image decreases. Thus, the final expression for gain computation at every iteration is written as

$$\lambda_i' = \lambda_i + c_1 \exp(-c_2 e^2); \quad (18)$$

where λ_i' is the adaptive gain; c_1 and c_2 are two constants defining the properties of gain adjustment; e is the mean distance in pixels between points in desired and current positions.

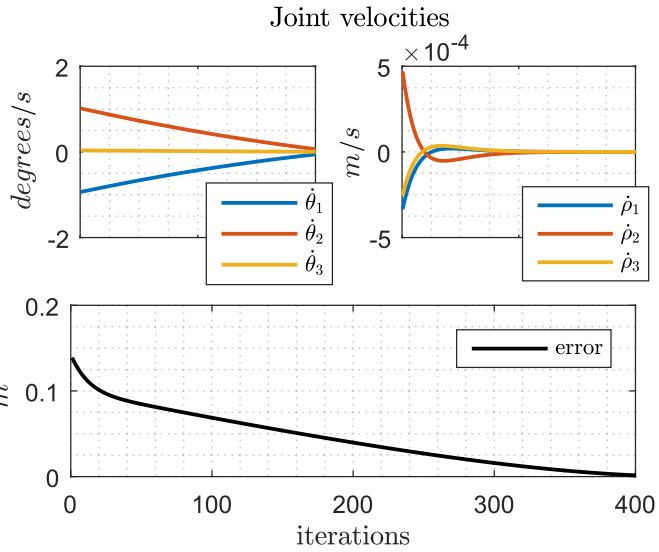

Fig. 3. 3D positioning of the CTR. *Top*: Evolution of joint velocities. *Bottom*: Evolution of the error.

IV. Experimental Results

A. Experimental Setup

For the experimental validation, the prototype presented in Fig. 4 is used. The robot is controlled with computer 1 (a 2.33 GHz Xeon Intel CPU). Computer 2 (a 3.4 GHz Intel Core TM) is exclusively dedicated to visual servoing tasks: image grabbing and processing, as well as computation of joint velocities. The latter are then sent to computer 1 asynchronously using an UDP protocol. As mentioned previously, the system is mounted in an eye-in-hand configuration. This means that a camera (MISUMI[1] camera, Schaumburg, Illinois, United States) is fixed to the robot's tip (the camera weight is negligible and has no effect on the robot behavior). It produces images with resolution of 640 × 480 pixels with a frame-rate of 20 images per second. The geometric features of the three tubes used to fabricate our prototype are listed in Table I. The tubes – acquired in straight shape from Euroflex GmbH (Pforzheim, Germany) – are made of a super-elastic alloy of Nickel and Titanium (NiTi) with a Young's modulus of 75 GPa. Each tube is linked to a rotation stage, which is itself linked to a translation stage. Both motor types are

[1]http://fr.misumi-ec.com/

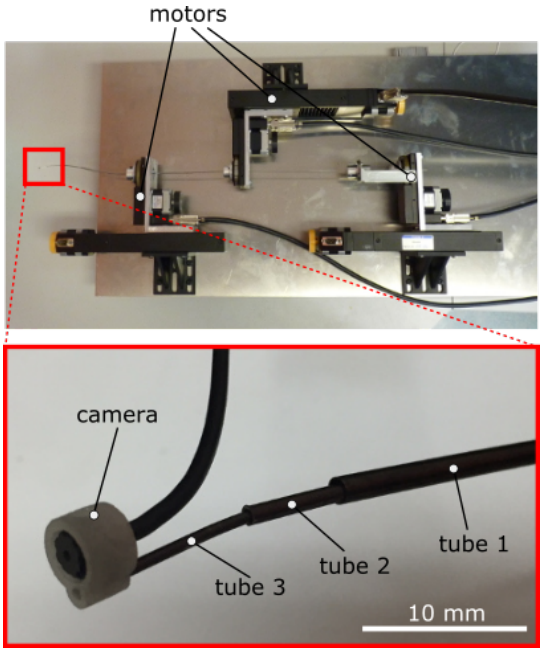

Fig. 4. Experimental setup of the 3-tube CTR. *Top*: General view of the setup, each motor controls two degrees of freedom, one rotation and one translation. *Bottom*: Zoom on the robot's end-effector with the miniaturized camera mounted on the tip of tube 3.

acquired from OWIS GmbH (Staufen im Breisgau, Germany). The specific curvatures were obtained by placing each tube at the desired length L_i inside of a mold containing patterned arc of circles. By using a metalworking furnace at 600°C during at least 20 minutes and quenching the part and fixture in room temperature water as described in [36], [37], the tubes keep the deformation in the desired shaped.

TABLE I
DESIGN PARAMETERS OF THE CTR PROTOTYPE.

Tube number	1	2	3
Curvature κ_i (m^{-1})	4.91	7.2	9.76
Length L_i (mm)	120	155	200
Outer diameter (mm)	3.112	2.032	1.32
Wall thickness (mm)	0.222	0.279	0.180
Transmission length (mm)	0	200±50	400±50

Three types of tests were realized to study the performance of the proposed control scheme: automatic CTR positioning, the same with adaptive gain, and a desired position in motion. All of them are described below.

B. Automatic CTR Positioning

1) 3 DOF Positioning: The first step allowing the validation of the discussed approach consisted in automatic positioning task of the CTR. The robot needed to perform a task of achieving the desired position from an arbitrary starting point. The target object is defined by four 2D geometric points (Fig. 5) that are then tracked during the operation. The model of the presented robot is now integrated in ViSP library and the main part of the code for the proposed visual servoing task is described in Listing 1. The results are shown in Fig. 5 and

Listing 1. Pseudo-code for visual servoing of CTR

```
//include ViSP files
#include <vpRobotRTC.h>

int main(){
  // Initialization
  vpRobotRTC robot;
  vpServo task;
  task.setServo(vpServo::EYEINHAND_L_cVe_eJe);
  vpDot2 dots[4];
  task.addFeatures(dots);

  bool task_finished = false;
  while (!task_finished) // visual servo loop
  {
    vpImage I = getImage();
    dots.track(I);
    vpColVector v = task.computeControlLaw();
    robot.setVelocity(vpRobot::ARTICULAR_FRAME, v);
    double error = task.getError().sumSquare();

    if (error < 1e-5) task_finished = true;
  }
}
```

Fig. 6. It can be noted that for two joint velocities $(\dot{\theta}_1, \dot{\rho}_1)$, it is decaying during the whole operation time. However, for the translation velocity $(\dot{\rho}_1)$ of tube 1, the curve is different which can be explained by high level of non-linearity of the robot forward kinematics. Nevertheless, the desired position is achieved with an error inferior to 10^{-5} m^2 in 40 iterations.

During the experiments, the effects of tube 2 on the control performances were negligible. Thus, we hold its translation and rotation constant and we limit the experimental validation to 3 DOF control.

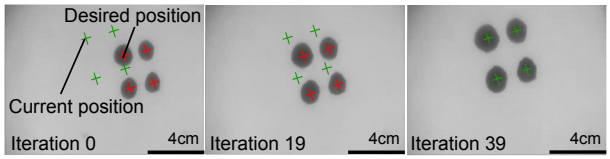

Fig. 5. Robot performing positioning task using IBVS. Images correspond to the experiment presented in Section IV-B1.

2) Adaptive gain test: In order to reduce the convergence time, the IBVS scheme with adaptive gain is tested. First, the constants c_1 and c_2 were determined experimentally. The constant c_1 defines the maximal value that can be added to the initial gain, thus, its maximal amplitude. The constant c_2 determines the starting point of adjustment. In other words, the value of error from which the adaptation takes effect. For example, for c_2 = 0.01, the adjustment starts from the error inferior to 25 pixels. In present work, we used c_1 = 80 and c_2 = 0.01. The results of positioning task performances are shown in Fig. 7. In contrast to the previous experiment with constant gains, the desired position is now achieved in 14 iterations, thus, three times faster. Moreover, the velocity of all joints tends to be exponentially decreasing.

3) Desired positions in motion: The last experiment presented here consists of testing the control scheme in case of time-varying desired positions (target in motion during the

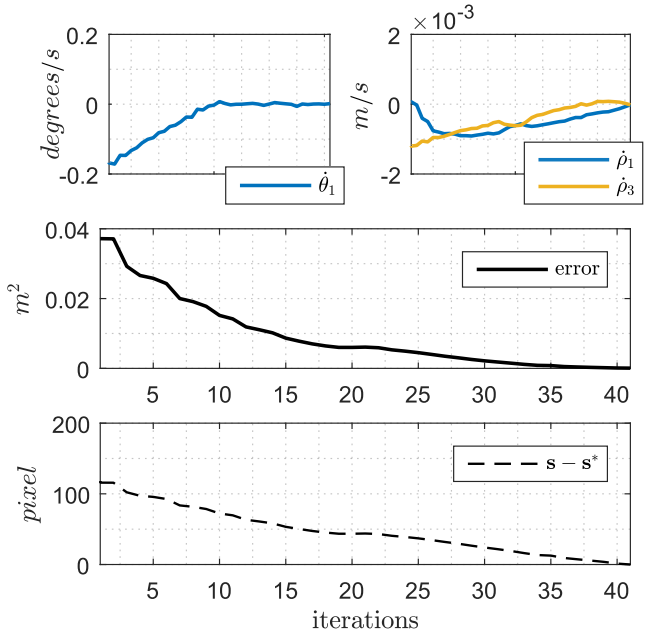

Fig. 6. 3D positioning of CTR. *Top:* Joint velocities. *Middle:* Evolution of the error. *Bottom:* Evolution of the error in the image.

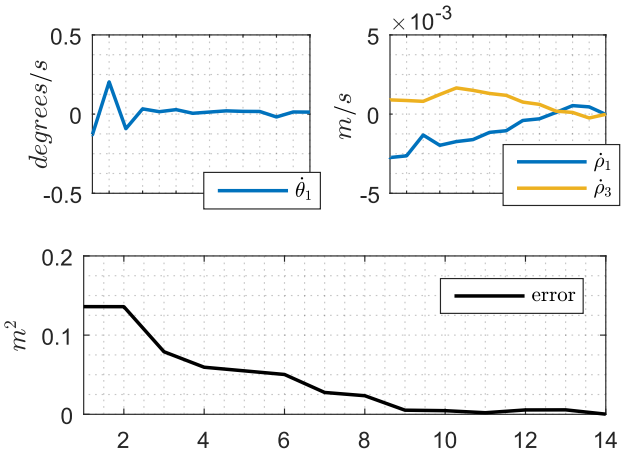

Fig. 7. 3D positioning of CTR with adaptive gain. *Top:* Joint velocities. *Bottom:* Evolution of the error.

positioning task achievement). Mainly, it corresponds to performing several consecutive positioning tasks while updating the desired position. As shown in Fig. 8, it can be noticed that the positioning error is maintained close to zero despite the variation of the desired positions. For instance, this can be useful for virtual compensation (in the image) of physiological movements during surgical interventions.

V. Conclusion

In this paper, we presented a model of a three-tube CTR including forward kinematics and Jacobian derivation. This allowed then to develop a new control scheme for such type of continuum robots based on IBVS techniques. Using a miniaturized camera mounted on the tip of the robot, thus serving as the robot's end-effector, it is now possible to control

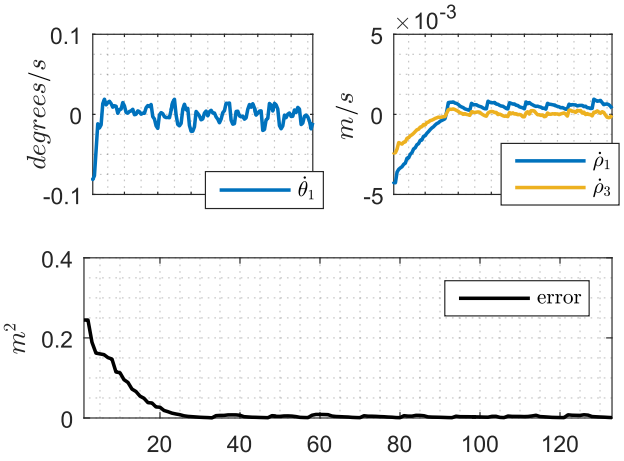

Fig. 8. CTR control using visual servoing with adaptive gain and desired positions in motion. *Top:* Joint velocities. *Bottom:* Evolution of the error.

the robot with high level of accuracy. In fact, the eye-in-hand configuration presents several advantages in contrast to more conventional setups with a static camera pointing toward the robot tool (eye-to-hand configuration). First, the robot is now capable to operate in a confined space as the camera moves with the robot. Secondly, it allows avoiding the problem of limited depth-of-field.

Further, the robot is automatically controlled using a visual servoing approach, which ensures accurate and repeatable tasks. The presented scheme was validated first in simulation and then on an experimental setup. The results are very promising as the final positioning error is below 10^{-5} m^2, or in other words, less than one pixel. Moreover, the implementation of adaptive gain allows not only reaching the desired position in fewer iterations but also to partly compensate the non-linearity of the robot model.

Finally, for the ease of future use, all presented algorithms were implemented within ViSP library. With two new developed classes, it will be possible to investigate the robot performances (repeatability, robustness, and stability). Future work will concern mostly the experimental part of this investigation. Firstly, it is important to extend the experimental validation to 6 DOF with medical scenarios. For this purpose, the target containing four black blobs for tracking may be replaced by one more similar to biological samples or robotic tool. Moreover, the white-light camera will be replaced by fiber-based optical biopsy like OCT and confocal microscopy, which will be co-axial with the CR's tubes. The ultimate idea is to be able to perform *in-situ* investigation by controlling the collection of optical biopsies of suspected tissue or organ.

References

[1] J. Burgner-Kahrs, D. C. Rucker, and H. Choset, "Continuum robots for medical applications: A survey," *IEEE Trans. on Robotics*, vol. 31, no. 6, pp. 1261–1280, 2015.

[2] H. B. Gilbert, D. C. Rucker, and R. J. Webster III, "Concentric tube robots: The state of the art and future directions," in *Int. Symp. Rob. Res.*, 2013, pp. 253–269.

[3] D. B. Camarillo, C. F. Milne, C. R. Carlson, M. R. Zinn, and J. K. Salisbury, "Mechanics modeling of tendon-driven continuum manipulators," *IEEE Trans. on Robotics*, vol. 24, no. 6, pp. 1262–1273, 2008.

[4] M. Cianchetti, T. Ranzani, G. Gerboni, I. De Falco, C. Laschi, and A. Menciassi, "Stiff-flop surgical manipulator: mechanical design and experimental characterization of the single module," in *IEEE/RSJ Int. Conf. on Intelligent Robots and Systems*, 2013, pp. 3576–3581.

[5] M. Farajollahi, V. Woehling, C. Plesse, G. T. Nguyen, F. Vidal, F. Sassani, V. X. Yang, and J. D. Madden, "Self-contained tubular bending actuator driven by conducting polymers," *Sensors and Actuators A: Physical*, vol. 249, pp. 45–56, 2016.

[6] M. T. Chikhaoui, and A. Cot, and P. Rougeot, and K. Rabenorosoa, and N. Andreff, "Design and Closed-loop Control of a Tri-layer Polypyrrole based Telescopic Soft Robot," *IEEE/RSJ Int. Conf. on Intelligent Robots and Systems*, 2016, pp. 1145–1150.

[7] Webster R.J., Swensen J.P., Romano J.M., Cowan N.J. "Closed-Form Differential Kinematics for Concentric-Tube Continuum Robots with Application to Visual Servoing". In *Experimental Robotics. Springer Tracts in Advanced Robotics*, vol 54. Springer, Berlin, Heidelberg, 2009.

[8] H. Su, G. Li, D. C. Rucker, R. J. Webster III, and G. S. Fischer, "A concentric tube continuum robot with piezoelectric actuation for MRI-guided closed-loop targeting," *Annals of Biomedical Engineering*, vol. 44, no. 10, pp. 2863–2873, 2016.

[9] I. S. Godage, A. A. Remirez, R. Wirz, K. D. Weaver, J. Burgner-Kahrs, and R. J. Webster, "Robotic intracerebral hemorrhage evacuation: An in-scanner approach with concentric tube robots," in *IEEE/RSJ Int. Conf. on Intelligent Robots and Systems*, 2015, pp. 1447–1452.

[10] C. Nadeau, H. Ren, A. Krupa, and P. Dupont, "Intensity-based visual servoing for instrument and tissue tracking in 3D ultrasound volumes," *IEEE Trans. on Automation Science and Engineering*, vol. 12, no. 1, pp. 367–371, 2015.

[11] Y. Baran, K. Rabenorosoa, G. J. Laurent, P. Rougeot, N. Andreff, and B. Tamadazte, "Preliminary results on OCT-based position control of a concentric tube robot," in *IEEE/RSJ Int. Conf. on Intelligent Robots and Systems*, 2017, pp. 3000-3005.

[12] M. Ourak, B. Tamadazte, and N. Andreff, "Partitioned camera-OCT based 6 DOF visual servoing for automatic repetitive optical biopsies," in *IEEE/RSJ Int. Conf. on Intelligent Robots and Systems*, 2016, pp. 2337–2342.

[13] J.-A. Seon, B. Tamadazte, and N. Andreff, "Decoupling path following and velocity profile in vision-guided laser steering," *IEEE Trans. on Robotics*, vol. 31, no. 2, pp. 280–289, 2015.

[14] G. Chesi, K. Hashimoto, D. Prattichizzo, and A. Vicino, "Keeping features in the field of view in eye-in-hand visual servoing: a switching approach," *IEEE Trans. on Robotics*, vol. 20, no. 5, pp. 908–914, 2004.

[15] J. Burgner, D. C. Rucker, H. B. Gilbert, P. J. Swaney, P. T. Russell, K. D. Weaver, and R. J. Webster, "A telerobotic system for transnasal surgery," *IEEE/ASME Trans. on Mechatronics*, vol. 19, no. 3, pp. 996–1006, 2014.

[16] H. Yu, L. Wu, K. Wu, and H. Ren, "Development of a multi-channel concentric tube robotic system with active vision for transnasal nasopharyngeal carcinoma procedures," *IEEE Robotics and Automation Letters*, vol. 1, no. 2, pp. 1172–1178, 2016.

[17] J. A. Piepmeier and H. Lipkin, "Uncalibrated eye-in-hand visual servoing," *The Int. J. of Robotics Research*, vol. 22, no. 10-11, pp. 805–819, 2003.

[18] Y. Lu, C. Zhang, S. Song and M. Q. H. Meng, "Precise motion control of concentric-tube robot based on visual servoing," in *IEEE Int. Conf. on Information and Automation*, 2017, pp. 299-304.

[19] K. Wu, L. Wu, C. M. Lim, and H. Ren, "Model-free image guidance for intelligent tubular robots with pre-clinical feasibility study: towards minimally invasive trans-orifice surgery," in *IEEE Int. Conf. on Information and Automation*, 2015, pp. 749–754.

[20] B. Espiau, F. Chaumette, and P. Rives, "A new approach to visual servoing in robotics," *IEEE Trans. on Robotics and Automation*, vol. 8, no. 3, pp. 313–326, 1992.

[21] G. Flandin, F. Chaumette, and E. Marchand, "Eye-in-hand/eye-to-hand cooperation for visual servoing," in *IEEE Int. Conf. on Robotics and Automation*, vol. 3, 2000, pp. 2741–2746.

[22] É. Marchand, F. Spindler, and F. Chaumette, "VISP for visual servoing: a generic software platform with a wide class of robot control skills," *IEEE Robotics & Automation Magazine*, vol. 12, no. 4, pp. 40–52, 2005.

[23] T. T. H. Tran and E. Marchand, "Real-time keypoints matching: application to visual servoing," in *IEEE Int. Conf. on Robotics and Automation*, 2007, pp. 3787–3792.

[24] N. Andreff, B. Espiau, and R. Horaud, "Visual servoing from lines," *Int. J. of Robotics Research*, vol. 21, no. 8, pp. 679–700, 2002.

[25] C. Collewet and E. Marchand, "Photometric visual servoing," *IEEE Trans. on Robotics*, vol. 27, no. 4, pp. 828–834, 2011.

[26] B. Tamadazte, N. Piat and E. Marchand, "A Direct Visual Servoing Scheme for Automatic Nanopositioning, " *IEEE/ASME Trans. on Mechatronics*, vol. 17, no. 4, pp. 728-736, 2012.

[27] L.-A. Duflot, A. Krupa, B. Tamadazte, and N. Andreff, "Shearlet-based vs. photometric-based visual servoing for robot-assisted medical applications," in *IEEE/RSJ Int. Conf. on Intelligent Robots and Systems*, 2016, pp. 4099–4104.

[28] M. Ourak, B. Tamadazte, O. Lehmann, and N. Andreff, "Wavelets-based 6 DOF visual servoing," in *IEEE Int. Conf. on Robotics and Automation*, 2016, pp. 3414–3419.

[29] R. J. Webster III and B. A. Jones, "Design and kinematic modeling of constant curvature continuum robots: A review," *The Int. J. of Robotics Research*, vol. 29, pp. 1661–1683, 2010.

[30] M. T. Chikhaoui and K. Rabenorosoa, and N. Andreff, "Kinematics and performance analysis of a novel concentric tube robotic structure with embedded soft micro-actuation," *Mechanism and Machine Theory* vol. 104, pp. 234–254, 2016.

[31] B. A. Jones and I. D. Walker, "A new approach to jacobian formulation for a class of multi-section continuum robots," in *Int. Conf. on Robotics and Automation*, 2005, pp. 3268–3273.

[32] R. M. Murray, Z. L. Li, and S. S. Sastry, *A Mathematical Introduction to Robotic Manipulation*, Eds, CRC Press, 1994.

[33] R. Hartley and A. Zisserman, *Multiple view geometry in computer vision*, Cambridge university press, 2003.

[34] O. Takayuki, C. Staub, and A. Knoll. "Framework of automatic robot surgery system using visual servoing." *IEEE/RSJ Int. Conf. on Intelligent Robots and Systems*, 2010, pp. 1937-1842.

[35] A. Cherubini, F. Chaumette, and G. Oriolo. "An image-based visual servoing scheme for following paths with nonholonomic mobile robots." *10th Int. Conf. on Control, Automation, Robotics and Vision*, 2008, pp.108-113.

[36] H. Gilbert, and R. J. Webster III. "Rapid, reliable shape setting of superelastic nitinol for prototyping robots." *IEEE Robotics and Automation Letters* vol. 1, no. 1, pp. 98-105, 2016.

[37] Johnson Medical Components. Accessed on November. 8, 2016; *Nitinol Shape Setting [Online] Available: http://jmmedical.com/resources/251/Nitinol-Shape-Setting.html*